

Mechanical improvement of continuous steel microcable reinforced geopolymmer composites for 3D printing subjected to different loading conditions

Zhijian Li ^{a,b}, Li Wang ^{a,*}, Guowei Ma ^{a,b}

^a School of Civil and Transportation Engineering, Hebei University of Technology, 5340 Xiping Road, Beichen District, Tianjin, 300401, China

^b College of Architecture and Civil Engineering, Beijing University of Technology, 100 Pingleyuan, Chaoyang District, Beijing, 100124, China

ARTICLE INFO

Keywords:

3D concrete printing
Geopolymer composite
Mechanical property
Continuous micro-cable reinforcement

ABSTRACT

Sufficient reinforcement is crucial for three-dimensional (3D) printed concrete structures. In this study, continuous and simultaneous micro-cable reinforcing methods are investigated to accommodate the 3D flexible and automatic characteristics of additive manufacturing processes, and to satisfy the mechanical-property requirements for construction applications. Different manufacturing-related micro-reinforcements and printing configurations are designed for 3D printing cable-geopolymers. The specimens were subjected to three different types of loading conditions (compressive, shear, and tensile) to gain a better understanding of the composite behavior. The results revealed interesting behaviors: under compressive loadings, the confinement effect of the micro-cables is fundamental in producing additional strength, ductility, and toughness. The print path must be considered for determining the confinement levels. Micro-cables increase the compressive strength by 50.0% in a certain print path. The shear strength depends primarily on the geopolymer weak planes' directions between two filaments instead of the embedded cable reinforcements. The tensile response is primarily governed by the micro-cable reinforcements and the configurations, which depend on the print paths. In certain configurations, the micro-cables result in 158% and 43.8 times increase in tensile strength and strain, respectively. This study provides valuable insights into the behavior of 3D-printed geopolymers composites with micro-cable reinforcement, which is necessary for designing and manufacturing complex structures using this novel reinforcement method.

1. Introduction

Extrusion-based three-dimensional concrete printing (3DCP) involves the extrusion of a specific mortar through a nozzle in sequential layers along a predefined fabrication path by a computer-controlled positioning process without any formwork or subsequent vibration [1–3]. It is becoming popular owing to its advantages of cost effectiveness, fast construction, formwork-free, minimal labor, and increased flexibility for designing complex geometries [4–7]. Researchers have extensively studied various materials and techniques for 3DCP to promote its use in real-life engineering applications [8–17]. However, multiple questions associated with significant limitations of the technology have been posed, e.g., the quantification of printability [18], weak interfaces [13], mechanical anisotropy [19,20], and printing path design.

A recurring issue that must be resolved is the lack of reinforcement, especially when 3DCP is used in large-scale constructions [10,21,22]. Nonreinforcement of concrete materials and structures produce obvious brittle damage owing to their weak tensile and shear resistance capacities, which significantly reduces the safety and reliability of 3D-printed structures. Currently, printed concrete is only used in a compressed state or as load-free structures [23,24]. The continuous extrusion and laminated stacking processes of cementitious composites hinder the introduction of steel rebars and stirrups into structural components. Therefore, it is crucial to automatically and effectively reinforce printed concrete and subsequently apply this advanced technique to engineering practice.

In recent years, some methods have been proposed to combine tensile reinforcements with 3D-printed constructions to improve tensile strength and ductility [25–28].

* Corresponding author.

E-mail address: wangl1@hebut.edu.cn (L. Wang).

Table 1

Chemical composition of FA and GGBFS by mass ratio.

	Al ₂ O ₃	SiO ₂	CaO	Fe ₂ O ₃	K ₂ O	MgO	Na ₂ O	P ₂ O ₅	TiO ₂	MnO	SO ₃
FA	28.3	49.2	3.6	11.9	1.0	1.6	0.68	0.92	1.56	0.36	0.25
GGBFS	15.3	36.5	35.2	0.63	0.49	5.69	0.49	0.08	0.45	0.52	2.85

1.1. Short fiber reinforcement

Short fibers (such as carbon and basal) are used to prepare fiber-reinforced concrete (FRC) materials for reinforcement [29,30]. Dispersed microfibers are added in the mix before material deposition to strengthen the 3D-printed structures. Hambach et al. [31] developed carbon-fiber-reinforced 3D-printed cementitious composites with a flexural strength of 30 MPa, enabled through aligned fibers that were produced from the extrusion process. Ma et al. [19] investigated the mechanical improvement of aligned basalt-fiber-reinforced composites for extrusion-based printing. These results confirmed the feasibility of using dispersed fiber reinforcements to reinforce 3D-printed structures; however, these composites are limited to shrinkage control or small strain resistances and fail to function as reinforced concrete.

1.2. Mesh mold reinforcement

ETH Zurich proposed an innovative mesh mold reinforcement method for 3D printing, which is a digital fabrication process of building reinforced meshes and formwork simultaneously using a robotic system. The main feature of this method is a terminal processor assembled on a manipulator, which can automatically build 3D structures [32]. To adapt to the flexibility of the construction process, horizontal (vertical) steel bars can be arranged discontinuously. Cement-based composites are evenly filled into the steel mesh, and no spillover occurs under the restraint of the steel mesh. However, the bond between concrete and the steel mesh requires further testing and optimization.

1.3. External reinforcement

Asprone et al. [33] attempted to assemble a series of 3D printed hollow components with the help of external reinforcement anchorage, and constructed two beams about 3.0 m in length. The whole assembly enhancement of the structure is to connect the 3D printed blocks in series by means of anchoring and fixing the upper and lower outer surfaces of the printing structure. Then the riveting perpendicular to the printing plane is used to fix the reinforcement system on the upper and lower surfaces to form an overall reinforcement. The connection of vertical printing plane is fixed, and the steel bar and printing structure will be fixed by pouring high strength and high viscosity mortar in the follow-up. Pre-stressing reinforcement has been placed into already printed components through post placement and post-tensioning process [2]. Concrete is extruded around vertically placed steel reinforcement by two nozzles layer by layer [26]. Using 3D printed concrete as permanent formwork and placing conventional reinforcement, which is followed by the casting process once the printed formwork has cured [4].

1.4. 3D printing metallic/polymeric reinforcement

Francesco Colangelo et al. [34,35] presents the results of an experimental study on the flexural reinforcement of a geopolymer mortar through additively manufactured metallic rebars though electron beam melting. Cylindrical embossments on the lateral surface of rebars were observed and meanwhile remarkably improvement of interfacial bond strength of the analyzed mortar was validated. F. Fraternali et al. [36] have highlighted that the composite reinforced with metallic fibers perform two times higher capacity than that reinforced with photo-polymeric fibers. Viktor Mechtcherine et al. [27] 3D-printed steel

reinforcement for digital concrete construction through gas-metal arc welding. The 3D-printed rebar produces better ductility than conventional steel bar B500. Xu et al. [37] put forward an alternative approach for creating SHCC by applying 3D printed polymeric reinforcement meshes. The distinct multiple cracking behaviors of proposed composites were observed.

1.5. Microcable reinforcement

The four above-mentioned approaches can enhance the mechanical toughness of 3D-printed samples considerably; however, they fail to accommodate the 3D flexible and automatic characteristics of 3D concrete printing. The continuous and simultaneous entrainment of flexible reinforcements into the 3D printing process should be investigated to satisfy the mechanical-property requirements [38]. Lim et al. [39] presented a hybrid reinforcement approach using both short fibers and in-process steel cables for reinforcement, where a 290% increase in the flexural strength of 3D-printed concrete was reported. Freek P. Bos [40] proposed a hybrid down/back-flow nozzle to optimize the cable-concrete bond properties and the corresponding design was successfully applied in the printing of a full-scale bicycle bridge. Previously, we have proposed a promising approach to simultaneously entrain a continuous microsteel cable (1.2 mm) during a filament (12 mm) deposition process to form reinforced composites. The cooperation and optimization of the printing process of geopolymers with the cable embedding process have been explored and validated [41].

To gain a better understanding of cable-reinforced composite behavior, the mechanical behavior of the new geopolymer composite under different loading conditions are further investigated. In this study, five types of microcables are tested for preparing cable-geopolymer composites to determine the optimal one. The bonding property between a steel microcable and geopolymers is investigated through a pull-out test. The effect of three print configurations on the mechanical behaviors of a cable-geopolymer are assessed through compressive, shear, and tensile tests. The microcable reinforcement method improves both the automation degree of reinforcement and the mechanical bearing capacity and safety of printed structures, which is important for promoting the practical use of 3DCP.

2. Materials and methods

2.1. Geopolymer preparation for 3D printing

Based on previous studies, geopolymers are primarily manufactured from a two-part mixture comprising alkaline solutions and solid aluminosilicate precursors [42–45]. Geopolymers have previously been successfully used for 3D concrete printing [46,47]. For ease of implementing 3DCP, a one-part geopolymer similar to a “just add water” cementitious mixture was developed for 3D printing in this study. Class-F low-calcium fly ash (FA) was selected as the main binder because of its wide availability, appropriate silica and alumina composition, and reduced water demand. Ground granulated blast furnace slag (GGBFS) was used for setting the time control [48]. The chemical compositions of FA and GGBFS by mass ratio are shown in Table 1. Silica fume was included to modify the thixotropic and microstructure properties of the geopolymers. Penta sodium metasilicate (PSM) powder, used as an alkali activator, was mixed with a dry binder before water was incorporated. Sand with a maximum particle size of 1 mm was adopted as fine aggregate for suitability with the narrow print head and shrinkage

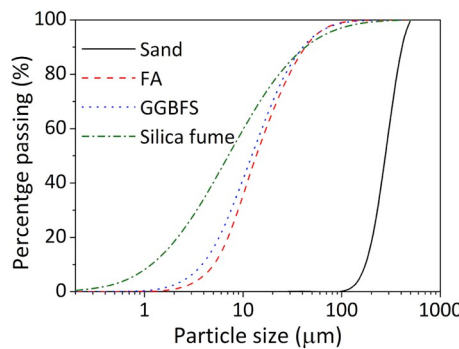


Fig. 1. Cumulative particle size distribution curve of sand, FA, GGBFS and silica fume.

Table 2
Mass ratio of the raw materials for 3D printable geopolymers.

Sand	GGBFS	FA	Silica fume	Water	PSM
1.2	0.25	0.64	0.11	0.348	0.125

control. The powders' particle size distribution is depicted in Fig. 1.

Table 2 presents the mixture proportion of the geopolymers used for 3D printing. For preparation, dry FA, GGBFS, silica fume, sand, and PSM were first stirred in a 50 L mixer for 5 min to obtain a uniform mixture; subsequently, water was added into the mixture and blended for an additional 3 min to achieve sufficient flowability. The measured open time and slump value were 30 min and 4.5 mm, respectively, which were within the limits recommended in our previous study [18]. Subsequently, the ready-mixed geopolymers were placed into the V-shape tank of the 3D printer for deposition.

2.2. Entrainment and optimization of micro-reinforcement

Fig. 2 shows the entraining process of micro-reinforcement in the geopolymer deposition processes. The ready mixed geopolymers are extruded out of the print head by rotating the blade in the V-shape tank.

Meanwhile, the continuous micro-reinforcement is feeding into the print head by an extruder, which is controlled by the step motor. However, the introduced micro-cables are prone to swaying in the extrusion due to the nozzle size is much larger than the cables. Consequently, the cables cannot be fixed at the center of geopolymer filaments and fail to produce effectively reinforcement. In response to these defects, one concentric tube is designed and inclined placed in the nozzle, and continuous cable is passed from the concentric tube in this method to prevent swaying and buckling. The cable feeding and geopolymer extrusion can automatically terminate at the same time through a special linkage device. When the printing of one layer is finished, both the geopolymer extrusion and cable feeding are simultaneous terminated, then the nozzle move up by a height of h (50 mm, enough for cutting device), and the cable is cut manually.

The entraining speed of the micro-reinforcement (v_e) coordinated well with the deposition speed (v_d) of the geopolymers. It was recommended that the deposition rate was equal to the pumping rate (v_p) of fresh materials.

$$v_e = \pi \times d \times N \quad (1a)$$

where v_e is the entraining speed of the cable (mm/s), d is the diameter of the extrusion gear (mm), and N is the stepper motor rotating speed (r/s).

$$v_d = \frac{\pi D^2}{4} v \quad (2a)$$

Here, v_d is the deposition rate (L/s), D is the nozzle diameter (mm), and v is the moving speed of the print head (mm/s).

$$v_p = 4 \times e \times d \times T \times n \quad (3a)$$

Here, v_p is the pumping rate of fresh materials (L/s), e is the eccentricity, d is the cross-section diameter of the rotor, T is the stator lead, and n is the main axle rotating speed of the used pump.

The desired reinforcements require sufficient compressive stiffness to facilitate the extrusion process through the micropipe. Additionally, it requires a low bending stiffness to accommodate flexible printing without penetrating the geopolymer filaments, especially when the printer head is required to turn at a geometrical curve or to climb from one layer to the next. To determine the optimal micro-reinforcement material for the preparation of a geopolymer composite, five types of

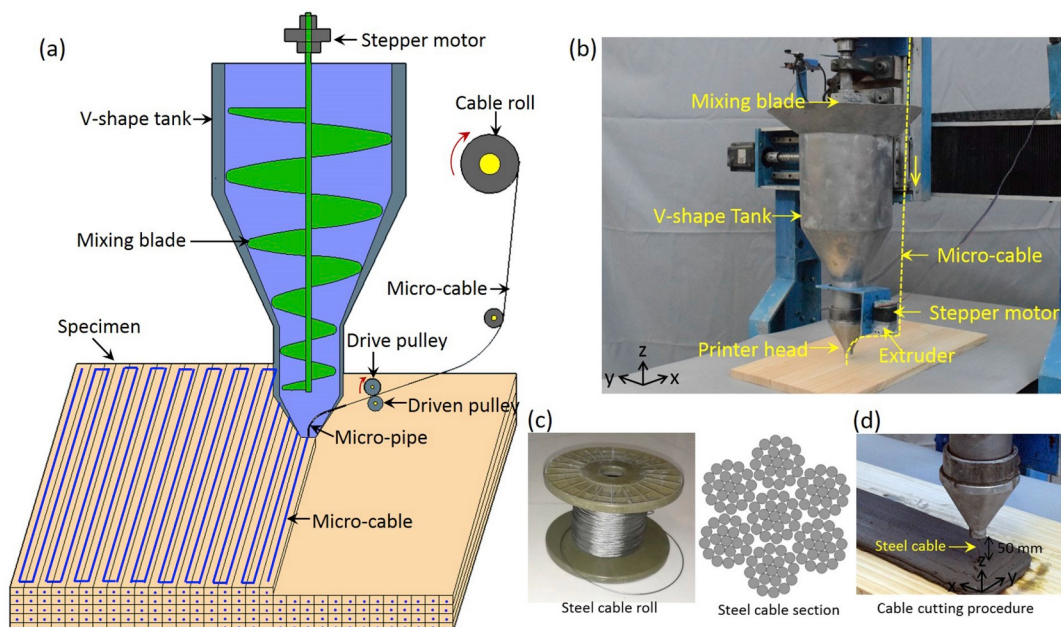


Fig. 2. (a) Schematic diagram and (b) real product of device of entraining micro-cable into geopolymer filaments. (c) Image of steel micro-cable and its cross section. (d) Cable cutting procedure.

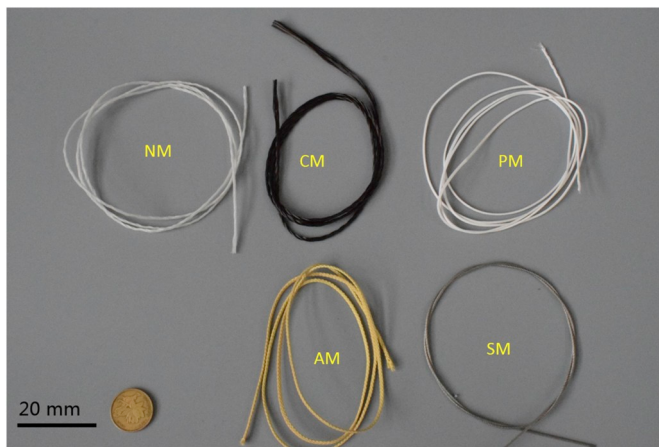


Fig. 3. Five different reinforcements for 3D printing.

Table 3
Physical and mechanical parameters of various cable reinforcements.

Reinforcement	Tensile capacity (N)	Size (mm)	Elongation	Elastic modulus (GPa)
Steel microcable (SM)	860	$\phi = 1.2$	40%	192
Nylon microcable (NM)	450	$\phi = 1.3$	19%	2.2
Carbon microcable (CM)	1500	$\phi = 1.4$	1.5%	235
Aramid microcable (AM)	1857	0.8×1.2	2.0%	110
Polyethylene microcable (PM)	2600	$\phi = 1.2$	3.6%	107

micro-cables were tested: nylon fiber, carbon fiber, PE fiber, aramid fiber, and steel cable (Fig. 3). The physical and mechanical parameters of each micro-reinforcement are listed in Table 3.

Without using a geopolymer, the five types of reinforcements can be smoothly extruded from the print head without blockage or interruption. When a geopolymer is extruded into the print head together with reinforcements, the geopolymer matrix is extruded successfully (Fig. 4

(a)); however, the PM, AM, NM, and CM reinforcements knotted in the extruder, as shown in Fig. 4(b) and (c). This is because the soft cables cannot penetrate the paste and entwine near the extrusion die. After a few of attempts, a continuous steel micro-cable (SM) (Fig. 2(c)) of diameter 1.2 mm is extruded from the print head together with the geopolymer successfully because it is hard under compressive stress and soft under bending stress. Each steel micro-cable has 7 shares, and each share has 19 strands. Moreover, a round nozzle of diameter 15 mm is used to ensure the small curvature of the steel micro-cable during printing. After a series of trials and errors, the entraining speed of the steel micro-cable is set to be equal to the horizontal printing speed, i.e., 60 mm/s. Meanwhile, the height of each layer is designed to be 6 mm.

2.3. Specimen fabrication

Three different print paths were trialed to produce specimens of the same shape to understand the effect of print paths and reinforcement configurations, as shown in Fig. 5(a). The specimens were fabricated in a concentric path called “Path A,” and two crosshatch zigzag shapes called “Path B” and “Path C” (90° rotated to each other). For print Path A, the extrusion process of geopolymer and feeding of micro-cable are continuous during the moving of nozzle from the outer to the inner loops. The adopted micro-cable is of low stiffness with 7 × 19 structure (Fig. 2(c)), and only one continuous cable is entrained in each layer, which ensures the flexible of the micro-cable reinforcement process. “Path B” and “Path C” have an angle of 90° and 45°, respectively. The specimens prepared for the compressive, shear, and tensile tests were designed to measure 108 mm × 108 mm × 108 mm, 400 mm × 108 mm × 48 mm, and 400 mm × 108 mm × 18 mm, respectively. All specimens were sealed and stored at room for 24 h, and subsequently transported to a moist cabinet at 20 ± 1 °C and relative humidity of 95 ± 5% for 28 days. The specimens printed for mechanical testing were polished before testing and are shown in Fig. 5(b).

The pull-out test specimens as shown in Fig. 5(c) were fabricated as having five vertical layers (x-axis) and three horizontal layers (y-axis). A single steel micro-cable was automatically inserted into the center of the specimen (54 mm × 30 mm) according to the feeding procedure mentioned above, and the length of the steel micro-cable extending out of the specimen was 40 mm. After curing, the printed pull-out testing specimens were cut based on the designed embedment length L_e .

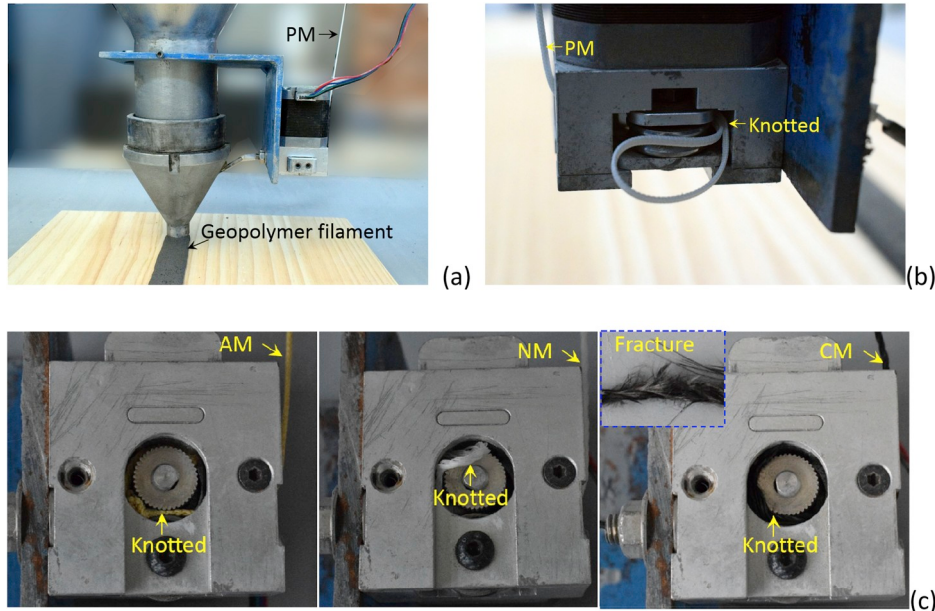


Fig. 4. Extruding (a) geopolymer successfully with (b) knotted PM reinforcement and (c) knotted AM, NM and CM reinforcement.

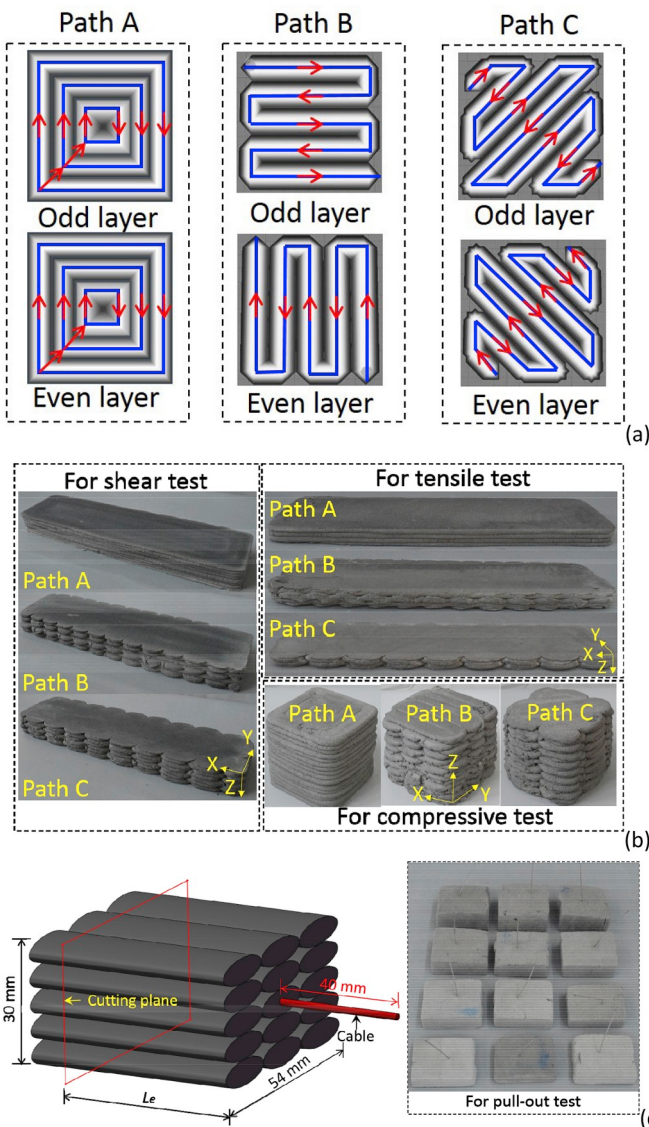


Fig. 5. (a) Print paths and (b) prepared specimens for mechanical properties test. (c) Specimens prepared for pull-out test.

3. Determination of the cable-geopolymer bonding property

A self-developed device, as shown in Fig. 6, was employed to determine the bonding between the cable and geopolymer matrix. The pull-out tests were performed using a universal testing machine equipped with a 20 kN load cell. An upward tensile load was applied to the steel micro-cable at a rate of 0.05 mm/min. The test rig grip was positioned as close as possible to the specimen. The wedge self-locking tension clamp ensured no slippage between the clamp and the micro-cables. The steel frame was of high stiffness and fixed on a table to restrict the movement of the geopolymer specimen. The load and displacement were measured and recorded once every second by an automatic data acquisition system. Four embedment lengths of the cable (L_e), i.e., 15, 25, 35, and 40 mm were designed to evaluate the bonding performances. The results were determined by averaging three identical specimens for each embedment length.

In the pull-out test, the stress distribution was not constant along the embedment length. Hence, the average bond strength is defined as follows:

$$\tau_{adh} = \frac{F_{adh}}{\pi d l} \quad (1b)$$

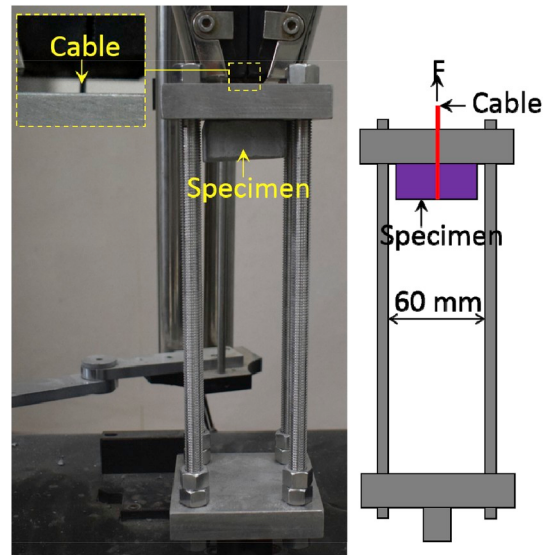


Fig. 6. Experimental set-up for pull-out test.

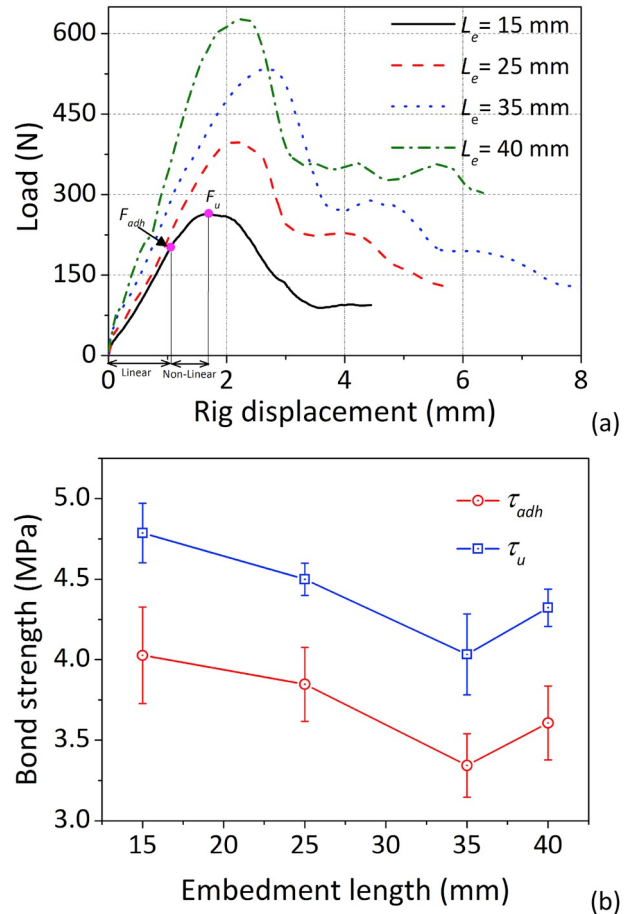


Fig. 7. (a) Load-displacement curves and (b) bond strengths of 3d printed specimens with different embedment lengths under pull-out test.

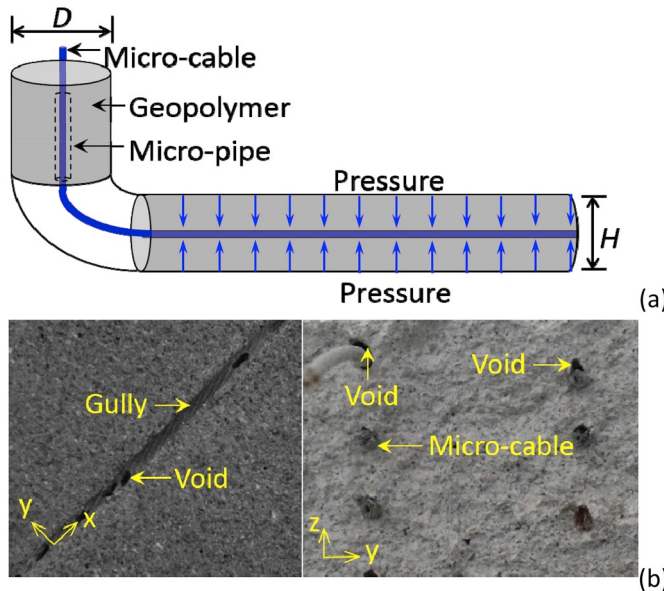


Fig. 8. (a) Schematic diagram of the inclusion process of steel micro-cable into geopolymers. Evidence for (b) contact between steel micro-cable and 3d printed geopolymers.

$$\tau_u = \frac{F_u}{\pi d l} \quad (2b)$$

where τ_{adh} and τ_u are the adhesive bond strength and ultimate bond strength (MPa), respectively; F_{adh} is the adhesive bond load (N); F_u is the ultimate bond load (N); d is the steel micro-cable diameter (mm); l is the embedment length (mm).

Fig. 7(a) depicts the average load–displacement curves for the pull-

out test. As shown, the linear stage first appears in the curves, and the adhesive bond capacity F_{adh} can be determined by the load value at the end of the initial linear, which is assumed to be determined by the cable-matrix adhesion solely. Subsequently, the curves proceed to the nonlinear deformation stage until failure, and the ultimate bond capacity F_u is determined by the load value at the peak of the load–displacement curve, which is determined by the combination of bond, dilatancy, and friction [49].

The average bond strengths between steel micro-cable and geopolymers for different embedment lengths are shown in Fig. 7(b). No obvious relationship exists among τ_u , τ_{adh} , and embedment length l , which is consistent with the results from Ref. [49]. The adhesive bond strength τ_{adh} varied from 3.34 to 4.00 MPa when the embedment length changes from 15 to 40 mm. Meanwhile, the ultimate bond strength τ_u varied from 4.03 to 4.79 MPa with different embedment lengths.

The basic anchorage lengths of the micro-cable-reinforced 3D-printed geopolymers l_{a1} can be calculated as follows:

$$l_{a1} = \frac{F_t}{\pi d \tau_u} \quad (3b)$$

where F_t is the tensile capacity of the steel micro-cable (N).

The basic anchorage length of a conventional casted reinforcement concrete l_{a2} can be calculated by Formula (4):

$$l_{a2} = \alpha \frac{f_1}{f_2} d \quad (4)$$

where α is the shape coefficient of steel reinforcement: 0.16 for smooth steel reinforcement, and 0.14 for ribbed steel reinforcement. f_1 is the tensile strength of steel reinforcement, and f_2 is the tensile strength of concrete. In this study, the value of f_1 is 335 MPa f_2 was 3 MPa, which was determined as 1/10 the values of the compressive strength.

The anchorage lengths of the micro-cable-reinforced 3D-printed geopolymers varied from $40d$ to $47d$. This was significantly larger than

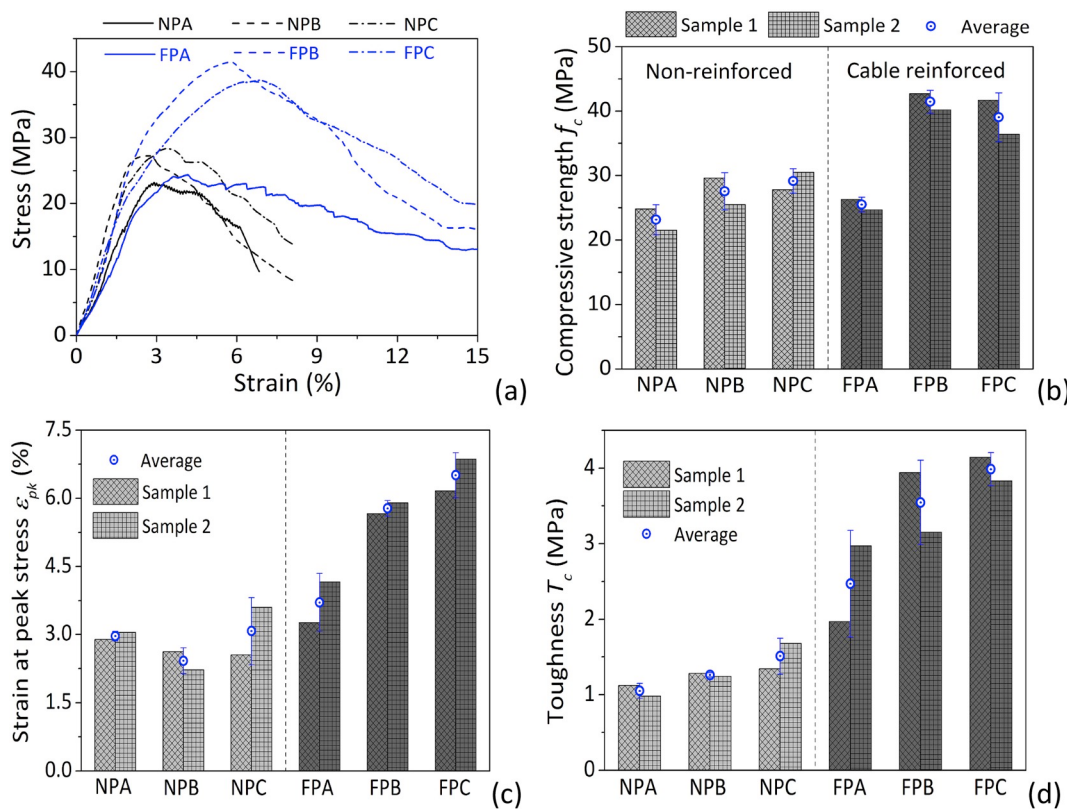


Fig. 9. (a) Compressive stress-deformation curves, (b) compressive strength, (c) strain at peak stress and (d) toughness of 3d printed geopolymers composites.

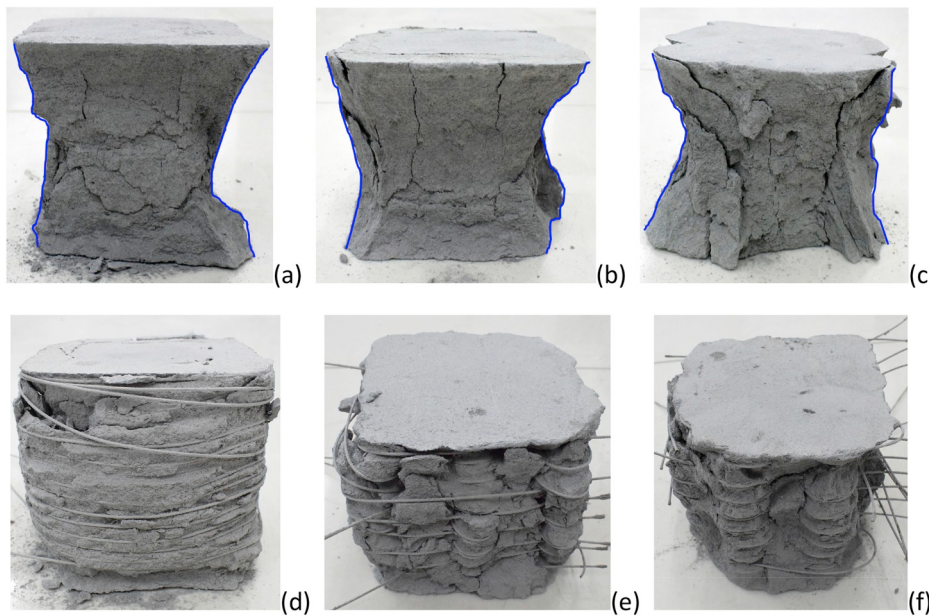


Fig. 10. Typical failure mode of specimens of (a) NPA, (b) NPB, (c) NPC, (d) FPA, (e) FPB and (f) FPC under compressive stress.

that of traditional casted reinforced concrete (RC), which was calculated to be $18d$ and $16d$ for smooth steel and ribbed steel reinforcements, respectively. Therefore, the cable reinforcements require longer anchorage lengths than traditional reinforcements. This is because the diameter of a micropipe is designed to be larger than that of a steel micro-cable to ensure the smooth feeding of steel micro-cables during 3D printing (Fig. 8(a)). Fig. 8(b) showed the poor bonding property between a steel micro-cable and geopolymer even though the extrusion pressure compacted the geopolymer and cables. The small surface area and smooth surface of the micro-cable may have necessitated the requirement for anchorage lengths that are longer compared to those of conventional reinforcements.

4. Mechanical properties assessment of cable-geopolymers

4.1. Evaluation of compressive performance

The compressive tests were performed at room temperature. After 28 days of curing, the prepared cubic specimens were subjected to vertical compressive loading by a universal servo-hydraulic testing system of capacity 2000 kN. The specimens were compressed at a rate of 0.05 mm/min. The applied load together with the corresponding displacement were recorded four times per second during the test. Furthermore, toughness was regarded as the area under the stress-strain curve before the load was reduced to 50% of the peak load [50].

As shown from the average stress-strain curves in Fig. 9(a), all printed specimens exhibited a strain-softening behavior and the printed specimens without a steel microcable exhibited post-peak deformation because flaws and pores were included during the printing. The NPB and NPC specimens indicated higher elastic stiffness and strength compared with NPA owing to the more even distribution of flaws in their microstructures. The specimens exhibited higher strength and larger post-peak deformation when continuous steel microcables were introduced.

As shown in Fig. 9(b), the compressive strengths f_c of specimens NPA, NPB, and NPC were 23.2, 27.6, and 29.2 MPa, respectively. Specimen NPC indicated the highest f_c , which was 25.9% and 5.8% higher than those of NPA and NPB. The f_c of specimens FPA, FPB, and FPC were 25.5, 41.5, and 39.1 MPa, respectively. Specimen FPB indicated the highest strength, which was 62.7% and 6.1% higher than those of FPA and FPC, respectively. Generally, f_c is enhanced by the addition of steel microcables. The compressive strengths of cable-reinforced specimens

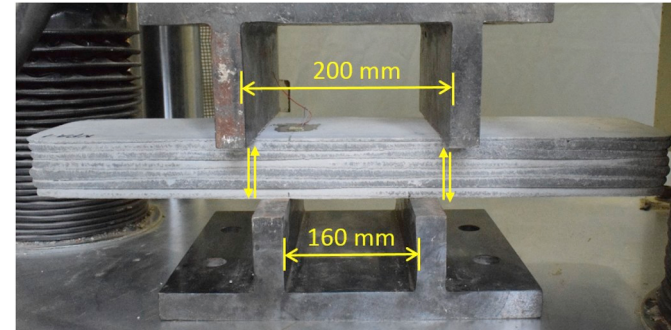


Fig. 11. Experimental set-up for shear test.

fabricated with paths A, B, and C were 50%, 34%, and 10% higher than those of noncable geopolymers, respectively.

Fig. 9(c) shows the strain at peak stress ϵ_{pk} of 3D-printed specimens with and without steel microcables. As shown, the ϵ_{pk} of NPC is 3.7%, which is 27% larger than that of NPA and NPB. The ϵ_{pk} of FPC is 75% and 12.6% larger than those of FPA and FPB, respectively. The ϵ_{pk} of specimens prepared with path B increased by 138.8% followed by that with path C (113.6%) when the steel microcable was incorporated; however, the increase using path A was by only 24.9%.

The compressive toughness T_c is calculated by the area under the stress-strain curve when the load is reduced to 50% of the peak load, as shown in Fig. 9(d). The steel microcable significantly improves the T_c , as a result of the energy absorption during the pull-out process of the steel microcables. The T_c of specimens with steel microcables prepared with paths A, B, and C were 135.2%, 181.7%, and 164.2% higher than those of corresponding specimens without steel microcables.

Fig. 10 shows the compressive failure status of the 3D-printed specimens. The nonreinforced specimens exhibited a brittle failure mode similar to ordinary concrete specimens, where two failure planes extend from the top and bottom edges to the center of the specimen (Fig. 10(a–c)). The outer part of the steel-microcable-reinforced geopolymer was peeled off and the steel microcable was pulled out from the geopolymer under compressive stress, thereby improving the ductile and energy absorption capacity (Fig. 10(d–f)).

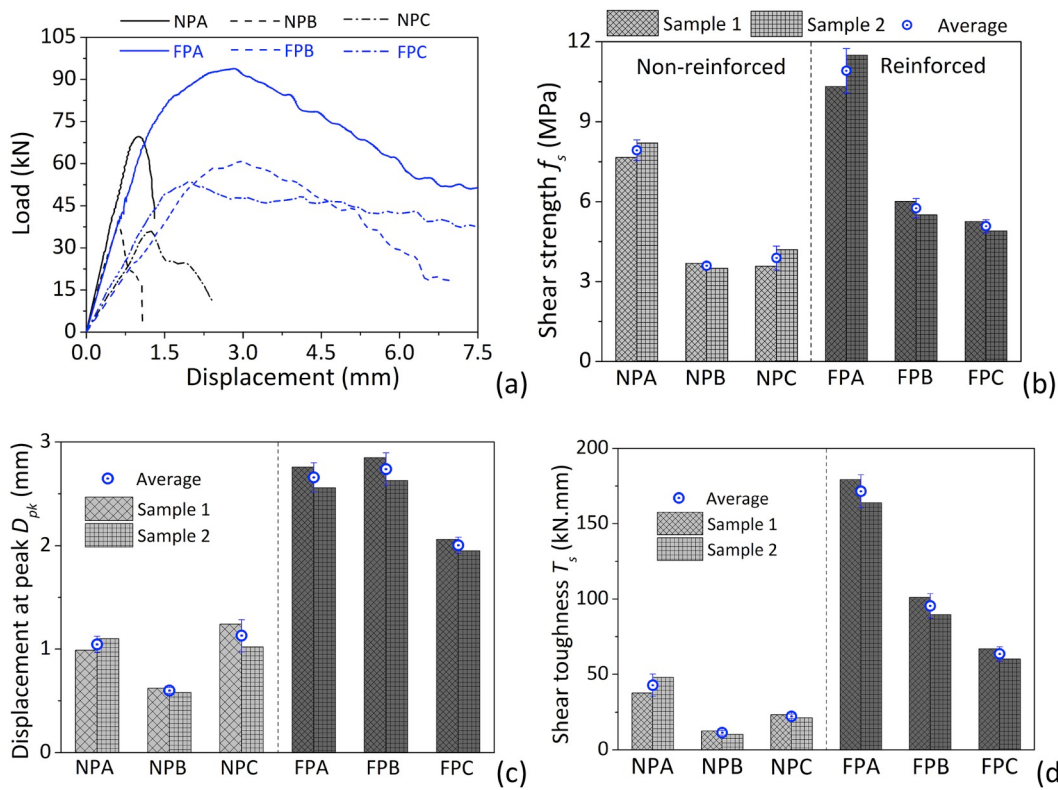


Fig. 12. (a) Shear load-displacement curves, (b) strength, (c) displacement at peak and (d) toughness of 3d printed geopolymers composites.

4.2. Evaluation of shear performance evaluation

As shown in Fig. 11, the rectangular beams were subjected to a “pure” shear stress using a 50 kN load cell at the displacement rate of 0.1 mm/min until failure occurred [51]. Shear stresses are produced by the relative movement between the top and bottom loading frames, both of which have two loading plates of wall thickness 15 mm. The internal spaces between the top two loading plates and the bottom ones are 200 and 160 mm, respectively. The generated shearing force is perpendicular to those of the printed layers as well as to the alignment of the embedded cables. The testing machine was connected to a computer to record four readings per second during the test. The shearing strength is calculated as follows:

$$f_s = \frac{F_{s,\max}}{2bh} \quad (5)$$

where \$f_s\$ is the shearing strength (MPa); \$F_{s,\max}\$ is the peak shear load (N); \$b\$ and \$h\$ are the measured width (mm) and height (mm) of the 3D-printed specimen, respectively.

The shear test results of the 3D-printed geopolymers composites with and without steel microcables are shown in Fig. 12. The elastic stiffness is reduced by the inclusion of steel microcables, as the steel microcables

have a lower shear stiffness compared with the geopolymer matrix (Fig. 12(a)). The steel-microcable-reinforced specimens exhibit a longer nonlinear stage than the corresponding nonreinforced specimen owing to their higher shear strengths compared with the geopolymer matrix. The load-displacement curve of the nonreinforced specimens plunged rapidly after the peak load, whereas the steel-microcable-reinforced specimens exhibited a large post-peak deformation, indicating ductile failure.

The shear strengths of the printed specimens with the same print path demonstrated similar shearing capacities, indicating the insignificant effect of the reinforcement of embedded cables on the shearing strength. Meanwhile, the weak interfaces produced by the printing paths significantly affected the shearing behaviors because cracks tended to initiate and accumulate at interfaces. As shown in Fig. 12(b), specimens NPA exhibited the highest load resistant capacity owing to most of their interlayer flaws being oriented perpendicular to the shear loading directions. The \$f_s\$ of NPA is 7.93 MPa, which is 122% and 104% higher than those of NPB and NPC, respectively. FPA indicates the highest \$f_s\$ of 10.91 MPa, which is 89% and 114% higher than those of FPB and FPC, respectively, because all the steel microcables in FPA are perpendicular to the shear loading direction.

The inclusion of steel microcables increases the shearing

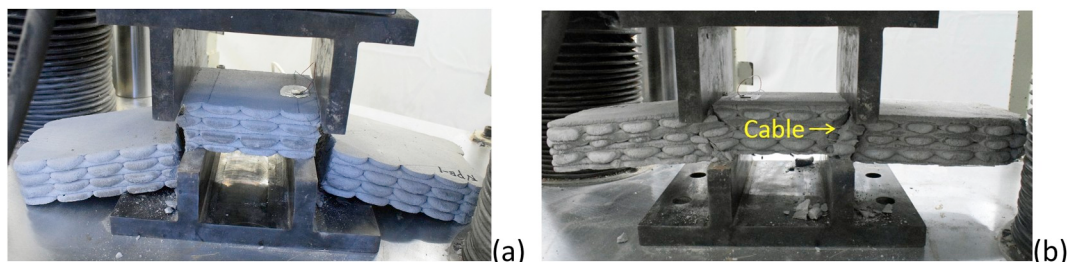


Fig. 13. Typical failure status of 3D printed geopolymers under shear stress: (a) NPB, (b) FPC.

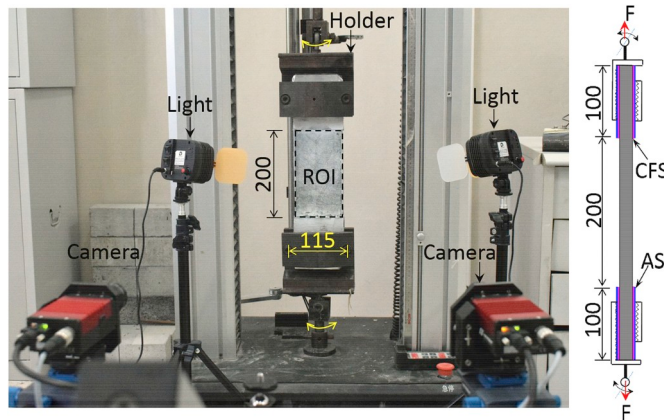


Fig. 14. Experimental set-up for tensile test.

deformation capacity D_{pk} of specimens prepared with paths A, B, and C by 153.3%, 356.7%, and 77.9%, respectively (Fig. 12(c)). As shown in Fig. 12(d), the shear toughness T_s of specimens prepared with paths A, B, and C are 3.0, 7.2, and 1.9 times higher than those of the noncable samples, respectively.

and C are 3.0, 7.2, and 1.9 times higher than those of the noncable samples, respectively.

Fig. 13 shows the failure status of the 3D-printed geopolymers under shear stress. For the nonreinforced specimens, large cracks were formed through the shear loading planes, and the specimens were broken into three sections (Fig. 13(a)), indicating obvious brittle failure. Meanwhile, for the reinforced specimens, the geopolymers near the shear loading planes was peeled off and the steel microcables were pulled out (Fig. 13(b)). Furthermore, the reinforced specimens exhibited integrity without collapse through a large shear diastrophism, which indicated a ductile failure mode.

4.3. Evaluation of tensile performance

Direct tensile tests with a fixed boundary setup were conducted on 3D-printed specimens with various print configurations, as presented in Fig. 14. First, a carbon fiber sheet and an aluminum sheet were glued to both ends of the specimens using epoxy resin. Subsequently, the specimens were fixed at the loading equipment using a self-developed holder, which could rotate in and out of the loading plane to ensure the appropriate axial tension for all specimens. Then, uniaxial tensile tests

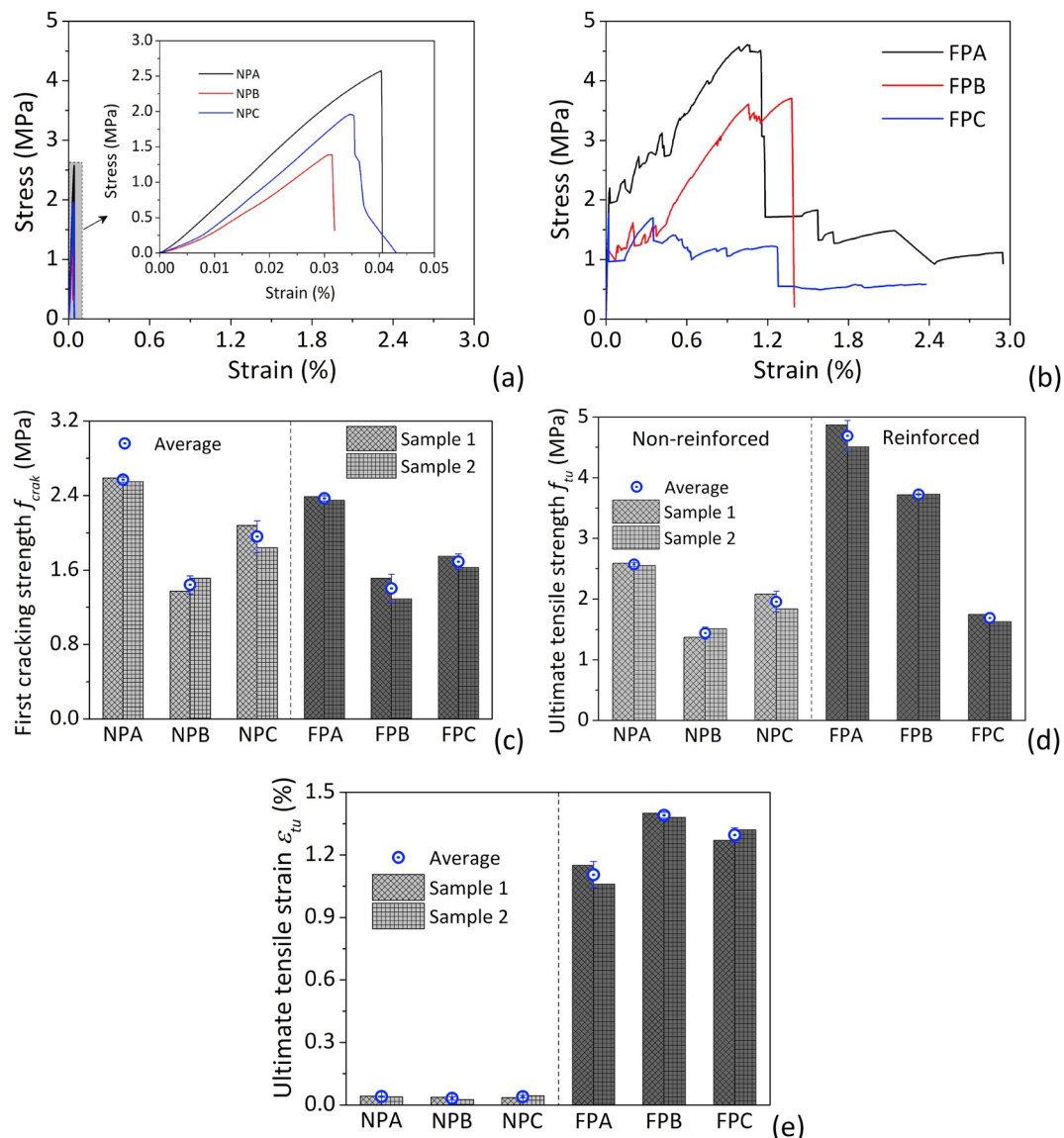


Fig. 15. Tensile stress-strain curves of (a) plain specimens and (b) reinforced specimens. (c) First cracking strength, (d) ultimate tensile strength and (e) ultimate tensile strain of 3D printed geopolymers composites.

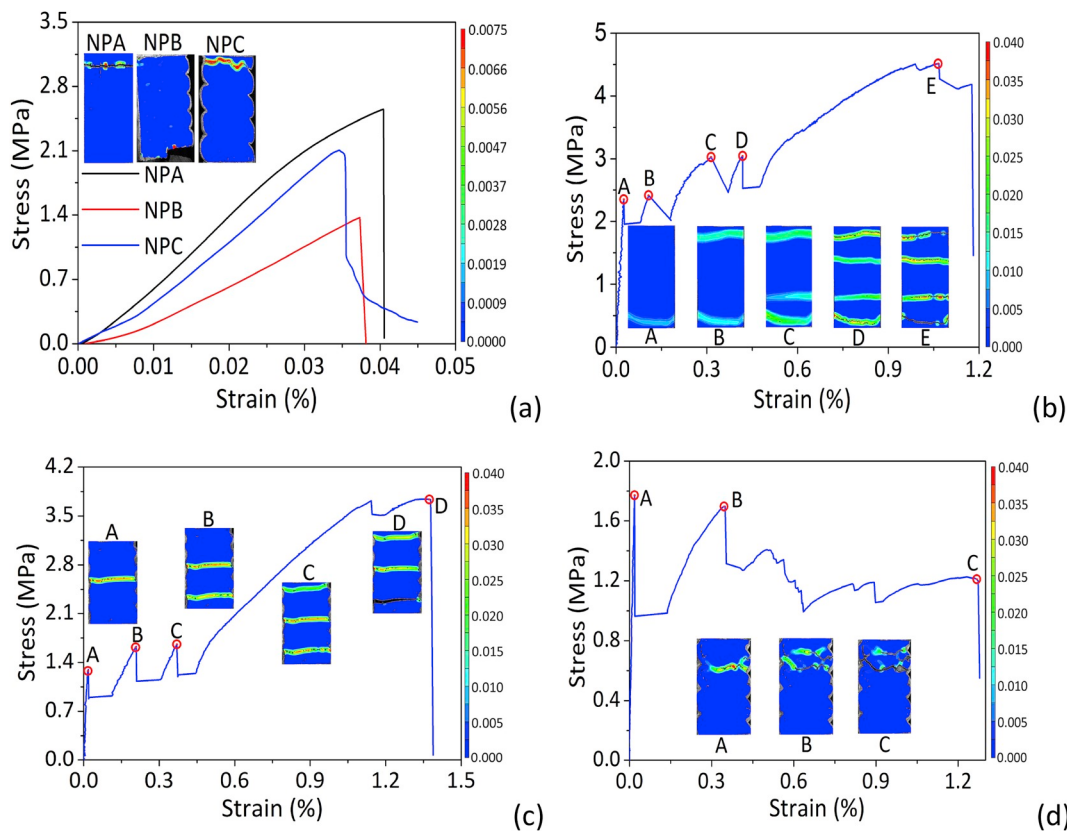


Fig. 16. DIC pictures for (a) non-reinforced specimen and reinforced specimen (b) FPA, (c) FPB and (d) FPC under tensile stress.

were performed in a testing machine of load capacity 20 kN in a deformation-controlled mode with a displacement rate of 0.05 mm/s until failure occurred. Meanwhile, the displacement and load were recorded once per second during the test.

As an optical and non-contacting technique, 3D digital image correlation was employed to monitor the deformation field and tensile crack pattern development in this study. The position and components related to this technique are shown in Fig. 14. To obtain the strain values, the specimens were first coated uniformly with a white non-reflective paint; subsequently, random speckle patterns of black spots were applied onto the specimen's surface at the region of interest (ROI). Then, two commercial CCD cameras of 8-bit intensity and effective resolution 3384×2704 pixels were connected to a camera controller software and placed in front of the printed specimens. Meanwhile, an artificial light source was placed in front of the specimens to improve the grayscale intensity of the captured images. Stereovision calibration was performed prior to testing, using a calibration plate provided by the manufacturer of the DIC system. Subsequently, the grey pictures of the speckle pattern at the ROI were captured every second. The displacement fields and hence the consequence strain fields were determined by comparing the subsequent speckle pattern pictures using the commercial 3D image correlation analysis software, Vic3D.

The relative deformation of two endpoints at the horizontal central axis of the AOI was extracted from the DIC results through the Vic3D software. The tensile strains were determined by dividing them by the corresponding lengths. Fig. 15(a) and (b) show the average tensile stress-strain curve of nonreinforced and steel-microcable-reinforced 3D-printed specimens, respectively. After the linear stage, the stress-strain curve of the nonreinforced specimens plunged rapidly, and an obvious brittle failure pattern was observed. Meanwhile, the stress-strain curves of the reinforced specimens exhibited many peak points and large tensile strains before the peak load was reached, indicating obvious ductile failure. Particularly, specimens FPA and FPB demonstrated strain-

hardening behaviors under tensile stresses.

The first cracking strength f_{crack} , ultimate tensile strength f_{tu} , and ultimate tensile strain ϵ_{tu} of the 3D-printed geopolymers composites with and without steel microcables are shown in Fig. 15(c)–(e), respectively. The f_{crack} of NPA, NPB, and NPC are 2.57, 1.44, and 1.96 MPa, respectively, which are the same as those of the corresponding f_{tu} . In addition, the f_{crack} of FPA, FPB, and FPC are 2.37, 1.40, and 1.69 MPa, respectively, which are similar to those of their corresponding nonreinforced specimens. This because the f_{crack} of the nonreinforced and reinforced specimens was determined primarily by the tensile strength of the geopolymers matrix instead of that of the steel microcable. Moreover, specimens prepared with path A exhibited the highest f_{crack} because most of their interlayer flaws that formed during printing was parallel to the tensile loading direction.

The f_{tu} of FPA, FPB, and FPC were 4.69, 3.72, and 1.69 MPa, respectively. The inclusion of steel microcables increased the f_{tu} by 82.5% and 158% for specimens prepared with paths A and path B, respectively, but reduced it by 13.8% for those prepared with path C. Particularly, the ϵ_{tu} increased significantly by the addition of steel microcables. The ϵ_{tu} of NPA, NPB, and NPC were 0.040%, 0.031%, and 0.040%, respectively, and it increased by 26.8, 43.8, and 31.5 times, respectively, with the inclusion of steel microcables to 1.110%, 1.390%, and 1.300%, respectively.

Fig. 16(a) shows the DIC pictures for the nonreinforced 3D-printed specimens after failure. Obvious main tensile cracks were observed near the loading end. Fig. 16(b)–(d) show the DIC pictures for the steel-microcable-reinforced 3D-printed specimens during loading. Multicrack patterns were observed and ductile failure was verified. Specimen FPA generated four small cracks gradually from both ends of the specimens to the center during testing. Specimen FPB exhibited three small cracks gradually from the center of the specimens to both ends. Meanwhile, specimen FPC exhibited two large cracks gradually near the end of the specimen. In particular, the cracks emerged simultaneously with the

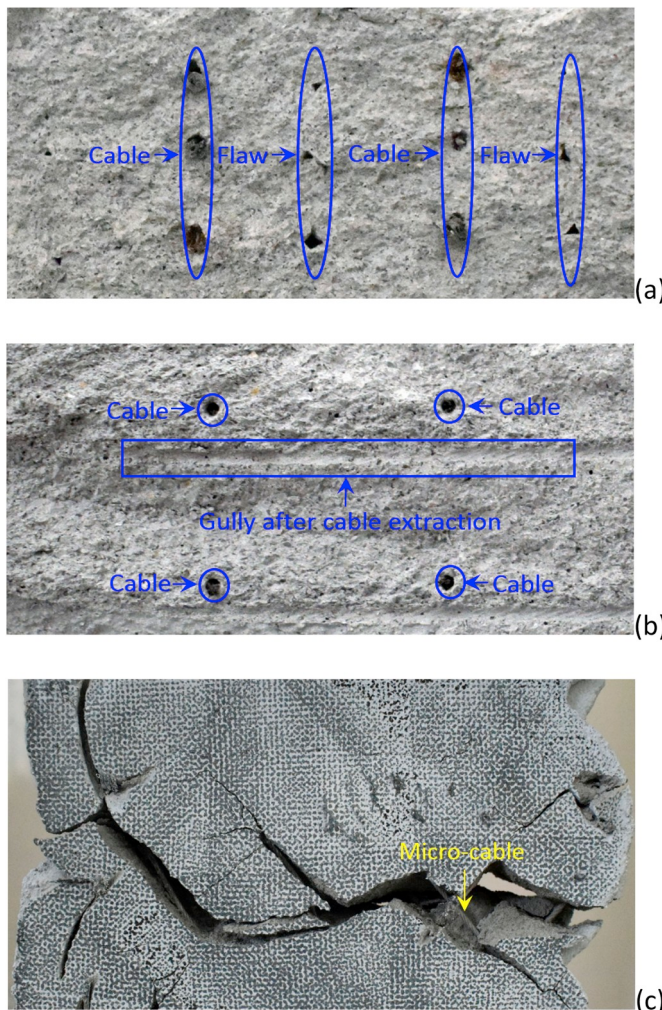


Fig. 17. Fracture of 3D printed steel micro-cable reinforced specimen (a) FPA and (b) FPB under tensile stress. (c) Steel micro-cable pulled out from specimen FPC under tensile stress.

peak points (e.g., A–E in Fig. 16(b)) of the stress–strain curve. This phenomenon can be explained by the following process. At the linear stages, both the geopolymer and steel microcables experienced tensile stresses and generated a consistent deformation. Subsequently, the first crack was incurred owing to the tensile failure of the geopolymer matrix, and the appearance of cracks was accompanied by the release of stress. Then, the tensile stress experienced by the failed geopolymer matrix was conveyed to the steel microcable and subsequently transferred to the undamaged geopolymer through the bonding stress between the steel microcable and geopolymer until the second crack was incurred.

The failure status of the steel-microcable-reinforced specimens were obtained using a high-resolution digital camera, as shown in Fig. 17. The steel microcable in specimen FPA is broken under tensile stress (Fig. 17(a)), and that the flaws are parallel to the steel microcable. The steel microcable parallel to the loading direction in specimen FPB is broken and that perpendicular to the loading direction is pulled out; subsequently, a gully is formed during the fracture after cable extraction (Fig. 17(b)). The interlayer shear transfer contributed partially to the tensile strength of the specimens. As shown in Fig. 17(c), the steel microcable in specimen FPC is pulled out from the geopolymer and bridges the cracks, thereby improving the ductility.

In general, the steel microcable is effective for enhancing the compressive, tensile, and shear properties of 3D-printed geopolymer composites; furthermore, it changes the failure mode from brittle to

ductile.

4.4. Effect of print configuration on mechanical behaviors

When exposed to shear loadings, the shear capacities of the printed specimens are primarily governed by the geopolymer composites than the embedded cable reinforcements. In terms of the printing configuration, the specimens will produce the weakest resistance when the weak planes are aligned with the shearing planes and the strongest resistance when the weak planes are perpendicular to the shear stresses.

Under compressive loading, the strength f_c and strain ε_{pk} development are primarily governed by the circumferential constraining force from the tensile-resistant steel microcables. According to Refs. [52,53], the compressive strength of the reinforced samples f_{cf} can be calculated using Eq. (6).

$$f_{cf} = f_c + 4.1\sigma_r \quad (6)$$

where f_c is the compressive strength of the nonreinforced samples and σ_r is the radial stress from microcable.

As depicted in Fig. 18(a), for print Path A, the confinement effect of the cable is primarily from the outer microcable reinforcement, and a lower percentage of the cable is subjected to tensile forces. Additionally, the microcable is discontinuous at the start point P for every layer, which can be pulled out easily under the circumferential expansion stress from compressive loading. σ_r is calculated by Eqs. (7)–(8)

$$\sigma_r = \frac{f_{cab}\rho_{cab}}{2} \quad (7)$$

$$\rho_{cab} = \frac{4A_{cab}D}{A_z h} \quad (8)$$

where f_{cab} is the ultimate strength of the cable; ρ_{cab} is the volumetric ratio of the cable; A_{cab} is the area of the cable; A_z is the area of the sample; D is the width of the sample and h is the layer height. f_{cf} is calculated to be 36.3 MPa in this study. The calculated strengths of the tested samples were higher for two reasons. First, the microcable was discontinuous at the start point P (Fig. 18(a)), which can be pulled out easily. Second, the ultimate strength f_{cab} of the cable is used to determine the improved compressive strength f_{cf} , which was overestimated for the undamaged microcables.

For print path B, every two layers is regarded as a calculation unit. The radial stress from the microcable σ_r is from those of seven cables in every calculation unit, and it is calculated using Eq. (9):

$$\sigma_r = \frac{7f_{cab}A_{cab}}{2hD} \quad (9)$$

The compressive strength of the reinforced samples f_{cf} is determined to be 47.1 MPa, which is higher than the test results.

For print path C, the radial stress from microcable σ_r is those from five cables in every layer, and it is calculated using Eq. (10):

$$\sigma_r = \frac{5f_{cab}A_{cab}}{\sqrt{2}hD} \quad (10)$$

The compressive strength of the reinforced samples f_{cf} is determined to be 46.8 MPa, which is also higher than the test results. For paths B and C, the lower strength of the tested samples is due to the overestimated tensile strength of the microcables.

Under tensile loading, the steel microcables parallel to the loading direction in specimens FPA and FPB are broken (Fig. 17), and the stress diagram is shown in Fig. 18(b). The ultimate tensile load F_{ut} and ultimate tensile strength f_{ut} are calculated as follows:

$$F_{ut} = f_{ut}A = Np_u \quad (11)$$

$$f_{ut} = \frac{F_{ut}}{A} = \frac{Np_u}{A} \quad (12)$$

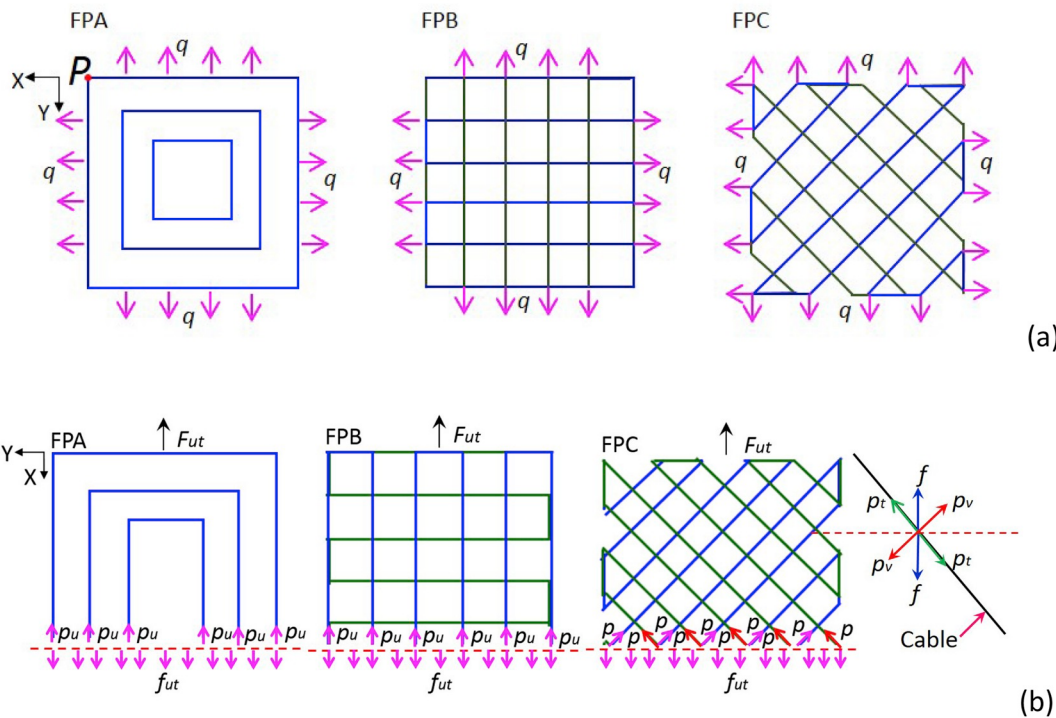


Fig. 18. Stress diagram for 3d printed steel micro-cable reinforced geopolymers under (a) compressive and (b) tensile loading.



Fig. 19. Application of micro-cable reinforced geopolymers for largescale 3D printing.

where A refers to the sectional area (mm^2). N is the number of steel microcables parallel to the loading direction in the section, which are 12 and 9 for specimens FPA and FPB, respectively, from the tensile test results. p_u is the ultimate tensile load of a single steel microcable (N).

Theoretically, from Eq. (5), the steel-microcable-reinforced specimens prepared with path A should yield the highest f_{ut} , i.e., 33% higher than that prepared with path B. However, it is 26.1% in practice owing to experimental errors. For the printing path C, as shown in Fig. 18(b), The tensile stresses that parallel to the cable p_t pullout the cables from the geopolymers. Additionally, the stresses vertical to the cables p_v separate the cable from the geopolymers, which reduce the bonding between the cable and geopolymers matrix. Therefore, printing path C is the easiest to be stripped and pulled out rather than broken (as shown in Fig. 17(c)). (as shown in Fig. 17(c)). And the steel micro-cable reinforced specimens prepared with path C perform the lowest f_{ut} .

Based on the aforementioned analysis, the introduced micro-cables

coupled with the printing configuration produce much larger influences on the mechanical performances than the weak interlayer flaws. Thus, it is necessary to optimize the print path before printing according to the actual stress status.

4.5. Microcable reinforced geopolymers composites for largescale 3D printing

It is promising to apply the proposed continuous cable reinforced geopolymers for application in largescale 3D printing. Fig. 19 shows the printing process of cementitious composite by real-time entraining micro cables in largescale robotic 3D printer. The printing span of the robotic is 3.3 m. The entraining speed shall be well coordinated to the deposition process of composites and moving speed of robotic arm. In this application case, circular nozzle with a diameter of 35 mm was used. The linear moving speed of robotic is set as 10 mm/s. This design was

deliberate to show the possibility and applicability of applying micro cable reinforced composite in largescale 3D printing structures.

5. Conclusion

This study provides a solution to simultaneously incorporate continuous steel cables into geopolymmer composite for reinforcement. The micro-cable reinforcement is embedded along the middle of the printing filament; hence the reinforcement configuration matches the printing paths. The 3D printed geopolymers exhibit complex composite behavior because the weak planes exist between layers and filaments and strong compressive strength is available in the printed direction. The following conclusions have been drawn from the current research:

- (1) Stiffness of the cable is an important consideration for this method of embedding reinforcements in printing filaments. Nylon, carbon fiber, aramid and Polyethylene cables with stiffness less than steel cables are found to knot and are not suitable for embedding in printing filament.
- (2) The confining action of the reinforcing cables are significant in increasing the compressive strength, strain at peak strength and toughness of the material. Some cable reinforcing configurations are more efficient in providing confinement than the others, and careful design of the printing path is important in achieving the required confinements.
- (3) The shear strength of the printed specimens is mainly governed by the geopolymers composite than the embedded cable reinforcements. The weak planes directions which is created by printing paths are significant in determining the shear strength of the printed specimens. When the weak planes align with the shear failure planes the weakest response is observed, and the strongest shear behavior is tested when the weak planes are perpendicular to the shear failure planes.
- (4) The tensile behavior is predominantly governed by the cable reinforcement configurations. The configurations that are aligned with the tensile loading directions performed well with multiple cracks with ductile behavior. And it performs the highest ultimate tensile strength of 4.69 MPa, which is 82.5% higher than that of the non-reinforced one. The interlayer shear transfer also contributes to some tensile strength of the specimens.
- (5) The pull-out test is done to investigate the bonding property between steel micro-cable and geopolymers. The adhesive bond strength varies from 3.34 to 4.00 MPa and the ultimate bond strength varies from 4.03 to 4.79 MPa with different embedment lengths. The cable reinforcements require long anchorage lengths compared to traditional reinforcements. This is likely to be due to the worse contact derived from the printing process and small size of the reinforcements (small surface area for bonding) and the smooth surface compared to ribbed surface found in conventional reinforcements.

Better understanding of cable reinforces geopolymers exposed to various loading conditions provides basic and vital knowledge necessary for the design of print paths for manufacturing complex structures. In order to improve the reinforcement role of micro-reinforcement, the cable-geopolymer adhesion properties have to be further enhanced by certain pre-treatment methods. Meanwhile, polymer-based cables are suggested to be explored to optimize the corrosion resistance than steel cables. Multi-cables introducing system is recommended to increase the reinforcing rate for real construction practices.

CRediT authorship contribution statement

Zhijian Li: Writing - original draft. **Li Wang:** Writing - review & editing. **Guowei Ma:** Project administration.

Acknowledgments

The authors wish to acknowledge the financial supports by the National Natural Science Foundation of China (Grant No. 51808183, No. 51627812 and No. 51878241), Hebei Science and Technology Department (No. 18391203D).

References

- [1] Panda B, Lim JH, Tan MJ. Mechanical properties and deformation behaviour of early age concrete in the context of digital construction. *Compos B Eng* 2019;165: 563–71.
- [2] Lim S, Buswell RA, Le TT, Austin SA, Gibb AGF, Thorpe T. Developments in construction-scale additive manufacturing processes. *Autom ConStruct* 2012;21: 262–8.
- [3] Zhang J, Wang J, Dong S, Yu X, Han B. A review of the current progress and application of 3D printed concrete. *Compos Appl Sci Manuf* 2019;125:105533.
- [4] Ngo TD, Kashani A, Imbalzano G, Nguyen KTQ, Hui D. Additive manufacturing (3D printing): a review of materials, methods, applications and challenges. *Compos B Eng* 2018;143:172–96.
- [5] De Schutter G, Lesage K, Mechtherine V, Nerella VN, Habert G, Agusti-Juan I. Vision of 3D printing with concrete — technical, economic and environmental potentials. *Cement Concr Res* 2018;112:25–36.
- [6] Wang L, Jiang H, Li Z, Ma G. Mechanical behaviors of 3D printed lightweight concrete structure with hollow section. *Arch. Civil Mech. Eng.* 2020. <https://doi.org/10.1007/s43452-020-00017-1>.
- [7] Buswell RA, Leal de Silva WR, Jones SZ, Dirrenberger J. 3D printing using concrete extrusion: a roadmap for research. *Cement Concr Res* 2018;112:37–49.
- [8] Li Y, Ma G, Wang L, Zhang J, Li Z. Real-time quantification of fresh and hardened mechanical property for 3D printing material by intellectualization with piezoelectric transducers. *Construct Build Mater* 2020;241:117982. <https://doi.org/10.1016/j.conbuildmat.2019.117982>.
- [9] Chen M, Li L, Zheng Y, Zhao P, Lu L, Cheng X. Rheological and mechanical properties of admixtures modified 3D printing sulphoaluminate cementitious materials. *Construct Build Mater* 2018;189:601–11.
- [10] Le TT, Austin SA, Lim S, Buswell RA, Law R, Gibb AGF, et al. Hardened properties of high-performance printing concrete. *Cement Concr Res* 2012;42(3):558–66.
- [11] Panda B, Ruan S, Unluer C, Tan MJ. Improving the 3D printability of high volume fly ash mixtures via the use of nano attapulgite clay. *Compos B Eng* 2019;165: 75–83.
- [12] Le TT, Austin SA, Lim S, Buswell RA, Gibb AGF, Thorpe T. Mix design and fresh properties for high-performance printing concrete. *Mater Struct* 2012;45(8): 1221–32.
- [13] Sanjaya JG, Nematollahi B, Xia M, Marchment T. Effect of surface moisture on inter-layer strength of 3D printed concrete. *Construct Build Mater* 2018;172: 468–75.
- [14] Chen Y, Chaves Figueiredo S, Yalcinkaya Ç, Çopuroğlu O, Veer F, Schlangen E. The effect of viscosity-modifying admixture on the extrudability of limestone and calcined clay-based cementitious material for extrusion-based 3D concrete printing. *Materials* 2019;12(9):1374.
- [15] Chen Y, Li Z, Chaves Figueiredo S, Çopuroğlu O, Veer F, Schlangen E. Limestone and calcined clay-based sustainable cementitious materials for 3D concrete printing: a fundamental study of extrudability and early-age strength development. *Appl Sci* 2019;9(9):1809.
- [16] Salman N, Ma G, Wang L, Wang F. A novel additive mortar leveraging internal curing for enhancing interlayer bonding of cementitious composite for 3D printing. *Construct Build Mater* 2020;118305. <https://doi.org/10.1016/j.conbuildmat.2020.118305>. In press.
- [17] Ji G, Ding T, Xiao J, Du S, Li J, Duan Z. A 3D printed ready-mixed concrete power distribution substation: materials and construction technology. *Materials* 2019;12 (9):1540.
- [18] Ma G, Li Z, Wang L. Printable properties of cementitious material containing copper tailings for extrusion based 3D printing. *Construct Build Mater* 2018;162: 613–27.
- [19] Ma G, Li Z, Wang L, Wang F, Sanjaya J. Mechanical anisotropy of aligned fiber reinforced composite for extrusion-based 3D printing. *Construct Build Mater* 2019; 202:770–83.
- [20] Ma G, Zhang J, Wang L. Mechanical characterization of 3D printed anisotropic cementitious material by the electromechanical transducer. *Smart Mater Struct* 2018;27(7). 075036.
- [21] Paul SC, Tay YWD, Panda B, Tan MJ. Fresh and hardened properties of 3D printable cementitious materials for building and construction. *Arch Civil Mech Eng* 2018;18(1):311–9.
- [22] Zhang Y, Zhang Y, She W, Yang L, Liu G, Yang Y. Rheological and harden properties of the high-thixotropy 3D printing concrete. *Construct Build Mater* 2019;201:278–85.
- [23] Xu J, Ding L, Love P. Digital reproduction of historical building ornamental components: from 3D scanning to 3D printing. *Autom ConStruct* 2017;76:85–96.
- [24] Gosselin C, Duballet R, Roux P, Gaudilliére N, Dirrenberger J, Morel P. Large-scale 3D printing of ultra-high performance concrete – a new processing route for architects and builders. *Mater Des* 2016;100:102–9.
- [25] Kreiger EL, Kreiger MA, Case MP. Development of the construction processes for reinforced additively constructed concrete. *Addit Manuf* 2019;28:39–49.

- [26] Asprone D, Menna C, Bos FP, Salet TAM, Mata-Falcón J, Kaufmann W. Rethinking reinforcement for digital fabrication with concrete. *Cement Concr Res* 2018;112: 111–21.
- [27] Mechtherine V, Grafe J, Nerella VN, Spaniol E, Hertel M, Füssel U. 3D-printed steel reinforcement for digital concrete construction – manufacture, mechanical properties and bond behaviour. *Construct Build Mater* 2018;179:125–37.
- [28] Katzer J, Szatkiewicz T. Properties of concrete elements with 3-D printed formworks which substitute steel reinforcement. *Construct Build Mater* 2019;210: 157–61.
- [29] Soltan DG, Li VC. A self-reinforced cementitious composite for building-scale 3D printing. *Cement Concr Compos* 2018;90:1–13.
- [30] Kaufmann J, Lübben J, Schwitter E. Mechanical reinforcement of concrete with bi-component fibers. *Compos Appl Sci Manuf* 2007;38(9):1975–84.
- [31] Hambach M, Volkmer D. Properties of 3D-printed fiber-reinforced Portland cement paste. *Cement Concr Compos* 2017;79:62–70.
- [32] Hack N, Lauer WV. Mesh-mould: robotically fabricated spatial meshes as reinforced concrete formwork. *Architect Des* 2014;84(3):44–53.
- [33] Asprone D, Auricchio F, Menna C, Mercuri V. 3D printing of reinforced concrete elements: technology and design approach. *Construct Build Mater* 2018;165: 218–31.
- [34] Farina I, Modano M, Zuccaro G, Goodall R, Colangelo F. Improving flexural strength and toughness of geopolymer mortars through additively manufactured metallic rebars. *Compos B Eng* 2018;145:155–61.
- [35] Farina I, Goodall R, Hernández-Nava E, di Filippo A, Colangelo F, Fraternali F. Design, microstructure and mechanical characterization of Ti6Al4V reinforcing elements for cement composites with fractal architecture. *Mater Des* 2019;172: 107758.
- [36] Farina I, Fabbrocino F, Carpenteri G, Modano M, Amendola A, Goodall R, et al. On the reinforcement of cement mortars through 3D printed polymeric and metallic fibers. *Compos B Eng* 2016;90:76–85.
- [37] Xu Y, Savija B. Development of strain hardening cementitious composite (SHCC) reinforced with 3D printed polymeric reinforcement: mechanical properties. *Compos B Eng* 2019;174:107011.
- [38] Ye W, Lin G, Wu W, Geng P, Hu X, Gao Z, et al. Separated 3D printing of continuous carbon fiber reinforced thermoplastic polyimide. *Compos Appl Sci Manuf* 2019; 121:457–64.
- [39] Lim JH, Panda B, Pham Q-C. Improving flexural characteristics of 3D printed geopolymers composites with in-process steel cable reinforcement. *Construct Build Mater* 2018;178:32–41.
- [40] Salet TA, Ahmed ZY, Bos FP, Laagland HL. Design of a 3D printed concrete bridge by testing. *Virtual Phys Prototyp* 2018;13(3):222–36.
- [41] Ma G, Li Z, Wang L, Bai G. Micro-cable reinforced geopolymers composite for extrusion-based 3D printing. *Mater Lett* 2019;235:144–7.
- [42] Zhou B, Wang L, Ma G, et al. Preparation and properties of bio-geopolymer composites with waste cotton stalk materials. *J Clean Prod* 2020;245:118842. <https://doi.org/10.1016/j.jclepro.2019.118842>.
- [43] Nematollahi B, Sanjayan J, Shaikh FUA. Synthesis of heat and ambient cured one-part geopolymers mixes with different grades of sodium silicate. *Ceram Int* 2015;41 (4):5696–704.
- [44] Zhao X, Liu C, Wang L, Zuo L, Zhu Q, Ma W. Physical and mechanical properties and micro characteristics of fly ash-based geopolymers incorporating soda residue. *Cement Concr Compos* 2019;98:125–36.
- [45] Zhao X, Liu C, Zuo L, Wang L, Zhu Q, Wang M. Investigation into the effect of calcium on the existence form of geopolymized gel product of fly ash based geopolymers. *Cement Concr Compos* 2019;103:279–92.
- [46] Panda B, Unluer C, Tan MJ. Extrusion and rheology characterization of geopolymers nanocomposites used in 3D printing. *Compos B Eng* 2019;176:107290.
- [47] Panda B, Singh GB, Unluer C, Tan MJ. Synthesis and characterization of one-part geopolymers for extrusion based 3D concrete printing. *J Clean Prod* 2019;220: 610–9.
- [48] Nematollahi B, Sanjayan J, Shaikh FUA. Matrix design of strain hardening fiber reinforced engineered geopolymers composite. *Compos B Eng* 2016;89:253–65.
- [49] Bos F, Ahmed Z, Jutinov E, Salet T. Experimental exploration of metal cable as reinforcement in 3D printed concrete. *Materials* 2017;10(11):1314.
- [50] Chen GM, He YH, Yang H, Chen JF, Guo YC. Compressive behavior of steel fiber reinforced recycled aggregate concrete after exposure to elevated temperatures. *Construct Build Mater* 2014;71:1–15.
- [51] Banthia N, Majdzadeh F, Wu J, Bindiganavile V. Fiber synergy in hybrid fiber reinforced concrete (HyFRC) in flexure and direct shear. *Cement Concr Compos* 2014;48:91–7.
- [52] Silva MAG. Behavior of square and circular columns strengthened with aramidic or carbon fibers. *Construct Build Mater* 2011;25(8):3222–8.
- [53] Lam L, Teng JG. Strength models for fiber-reinforced plastic-confined concrete. *J Struct Eng* 2002;128(5):612–23.